Hyper-phosphorylation of nsp2-related proteins of porcine reproductive and respiratory syndrome virus

Pengcheng Shang[a,1], Fangfeng Yuan[b], Saurav Misra[c], Yanhua Li[a,2], Ying Fang[a,b,*]

[a] Department of Diagnostic Medicine and Pathobiology, College of Veterinary Medicine, Kansas State University, Manhattan, KS, USA
[b] Department of Pathobiology, College of Veterinary Medicine, University of Illinois at Urbana-Champaign, Urbana, IL, USA
[c] Department of Biochemistry and Molecular Biophysics, Kansas State University, Manhattan, KS, USA

ABSTRACT

Viruses exploit phosphorylation of both viral and host proteins to support viral replication. In this study, we demonstrate that porcine reproductive and respiratory syndrome virus replicase nsp2, and two nsp2-related −2/−1 frameshifting products, nsp2TF and nsp2N, are hyper-phosphorylated. By mapping phosphorylation sites, we subdivide an extended, previously uncharacterized region, located between the papain-like protease-2 (PLP2) domain and frameshifting site, into three distinct domains. These domains include two large hypervariable regions (HVR) with putative intrinsically disordered structures, separated by a conserved and partly structured interval domain that we defined as the inter-HVR conserved domain (IHCD). Abolishing phosphorylation of the inter-species conserved residue serine[918], which is located within the IHCD region, abrogates accumulation of viral genomic and subgenomic RNAs and recombinant virus production. Our study reveals the biological significance of phosphorylation events in nsp2-related proteins, emphasizes pleiotropic functions of nsp2-related proteins in the viral life cycle, and presents potential links to pathogenesis.

1. Introduction

As the most common form of post-translational modification, phosphorylation is involved in every aspect of cellular processes, including signal transduction, gene transcription, protein translation, and substrate protein regulation, among others (Humphrey et al., 2015; Hunter, 1995; Johnson, 2009; Tarrant and Cole, 2009; Ubersax and Ferrell, 2007). It is estimated that up to 30% of the constituent proteins of the human proteome are modified by kinases (Ubersax and Ferrell, 2007). Protein kinases mediate the transfer of the γ-phosphate from ATP to specific residues (Ser, Thr, or Tyr) of target proteins (Humphrey et al., 2015; Hunter, 1995; Johnson, 2009; Tarrant and Cole, 2009; Ubersax and Ferrell, 2007). As intracellular pathogens that replicate exclusively in live cells, viruses modulate phosphorylation-regulated signaling pathways in host cells. Viruses also utilize host phosphorylation machinery to modify viral proteins in order to establish a productive life cycle (Keating and Striker, 2012; Keck et al., 2015). Phosphorylation of specific viral proteins regulates viral protein functionality, virus replication, and control of host cellular responses (Keating and Striker, 2012; Keck et al., 2015). In nidoviruses,

nucleocapsid (N) proteins of coronaviruses and arteriviruses have been shown to be phosphorylated, with potential impacts on viral RNA transcription (McBride et al., 2014; Wu et al., 2009; White et al., 2007; Surjit et al., 2005; Stohlman and Lai, 1979; Spencer et al., 2008; Peng et al., 2008; Mohandas and Dales, 1991; Chen et al., 2005; Chang et al., 2009; Calvo et al., 2005; Zeegers et al., 1976). However, whether other nidoviral proteins are phosphorylated and the functional consequences of such phosphorylation events remain largely uncharacterized.

Porcine reproductive and respiratory syndrome virus (PRRSV) is a leading viral pathogen that has caused significant economic loss to the global swine industry (Fang and Snijder, 2010; Snijder et al., 2013). PRRSV belongs to order *Nidovirales*, family *Arteriviridae*. Previously, PRRSV was divided into two distinct genotypes, European genotype (type 1) and North American genotype (type 2). Due to the substantial genetic difference in their sequences, the two genotypes were recently assigned to two distinct species, PRRSV-1 and PRRSV-2 (Kuhn et al., 2016). PRRSV contains a positive-sense (+) single-stranded (ss) RNA genome (Fang and Snijder, 2010; Snijder et al., 2013). The viral genome is approximately 15 kilobases (kb) in length and contains eleven known open reading frames (ORFs). The 3′-end ORFs encode
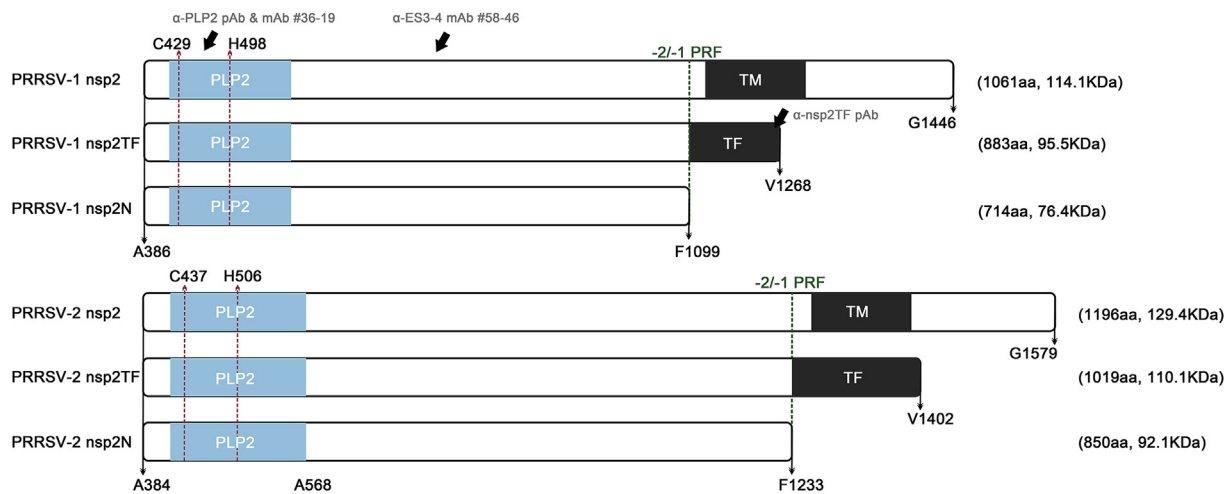
Fig. 1. Schematic diagram of PRRSV nsp2-related proteins. The nsp2, nsp2TF, and nsp2N proteins of PRRSV-1 (strain SD01-08, Genbank # DQ489311.1) and PRRSV-2 (strain SD95-21, Genbank # KC469618.1) shown with amino acid sequence length and predicted molecular weight. Positions of PLP2, catalytic dyad, and −2/−1 PRF site are indicated with amino acid numbers based on ORF1a or ORF1a′-TF of the corresponding PRRSV sequences. Specific mAb or pAb recognition sites are indicated with black arrows. PLP2, papain-like protease 2; −2/−1 PRF: −2/−1 programmed frameshifting site; TM: transmembrane domain; TF: nsp2TF C-terminal trans-frame region.

four membrane-associated glycoproteins (GP2a, GP3, GP4 and GP5), two non-glycosylated membrane proteins (E and M) and the nucleo-capsid protein (N) (Fang and Snijder, 2010; Snijder et al., 2013). The 5′ proximal three-quarters of the genome contain ORF1a and ORF1b, which encode two long polyproteins, pp1a and pp1ab (Fang and Snijder, 2010; Snijder et al., 2013).

The pp1a and pp1ab polyproteins are further proteolytically pro-cessed into 14 mature nonstructural proteins (nsps) after synthesis from the genomic RNA template (Fang and Snijder, 2010; Snijder et al., 2013). Four virus-encoded protease domains direct the proteolytic processing. These include two papain-like proteases (PLP1α and PLP1β) located in nsp1α and nsp1β, a papain-like protease (PLP2) domain lo-cated at the N-terminus of nsp2, and a serine protease (SP) located in nsp4. PLP1α autocleaves between nsp1α/nsp1β, PLP1β autocleaves between nsp1β/nsp2, and PLP2 cleaves between nsp2/nsp3. These autocleavage processes induce the rapid release of nsp1α, nsp1β and nsp2 from the polyprotein. Recently, we identified two novel nsp2-re-lated proteins, nsp2TF and nsp2N (Fang et al., 2012; Li et al., 2014). The nsp2TF is expressed through a −2 programmed ribosomal frame-shift (PRF) mechanism, which accesses an alternative ORF (TF) through a frameshifting site that overlaps the nsp2-encoding region. The re-sulting transframe fusion protein consists of the N-terminal two thirds of nsp2 followed by a unique C-terminal domain that is translated from the novel TF ORF. At the same frameshifting site, −1 PRF also occurs, in which the −1 PRF encounters an immediate stop codon to generate a truncated nsp2 protein, termed nsp2N. Nsp2, nsp2TF and nsp2N all contain the PLP2 domain and the following region located between the PLP2 domain and the frameshifting site. Other cleaved nsp2 variants of smaller protein size have also been reported (Han et al., 2010).

The nsp2 protein is the largest replicase cleavage product and contains multiple domains that serve multifunctional roles. Besides cleaving the nsp2/nsp3 site, the nsp2 functions as a cofactor for the SP to process the nsp3-12 region (Fang and Snijder, 2010). In addition, PLP2 is capable of removing ubiquitin (Ub) and Ub-like modifiers like ISG15 (an Interferon-stimulated gene) from host cell substrates (Sun et al., 2010, 2012; van Kasteren et al., 2012; Frias-Staheli et al., 2007). The C-terminus of nsp2 contains a highly conserved Cys-rich domain of unknown function as well as a multi-spanning transmembrane domain that plays a role in the formation of membranous structures that fa-cilitate viral replication (Fang and Snijder, 2010; Snijder et al., 2013). The central region of nsp2 (which is also present in nsp2TF and nsp2N) contains hypervariable sequences, in which various deletions/

insertions have been reported (Fang and Snijder, 2010; Snijder et al., 2013). Significantly, a cluster of immuno-dominant B cell epitopes and potential T-cell epitopes was identified within this region (Oleksiewicz et al., 2001; Fang et al., 2004). In particular, highly pathogenic PRRSV variants exhibit specific signature-like variations, raising the possibility of connections between nsp2 sequence hyper-variability and viral pa-thogenicity (Fang and Snijder, 2010; Snijder et al., 2013). However, the central region of nsp2 is poorly characterized in terms of its structure and function. In this study, we demonstrate that the PRRSV nsp2 and two nsp2-related PRF products, nsp2TF and nsp2N, are hyper-phos-phorylated. By combining phosphorylation site mapping, disorder analysis and protein structural prediction, we divided the central region of nsp2 into three distinct domains, located between the PLP2 domain and PRF site. We determined that the central region contains two large hypervariable regions (HVRs) with putative intrinsically disordered structures, separated by a conserved and partially structured interval domain that we defined as the IHCD (Inter-HVR Conserved Domain). Importantly, we identified a highly conserved phosphorylation site (Serine[918]) in the IHCD that is critical for viral replication. The results of our study expand the nidovirus phospho-proteome and reveal im-portant roles for the phosphorylation of nsp2-related proteins in the regulation of virus replication, as well as potential effects on viral pa-thogenesis.

2. Results

2.1. PRRSV nsp2-related proteins are hyper-phosphorylated

Based on the protein sequences, the predicted molecular weights of PRRSV-1 (strain SD01-08) nsp2-related proteins, nsp2, nsp2TF, and nsp2N, are 114 KDa, 96 KDa, and 76 KDa, respectively. The corre-sponding molecular weights in PRRSV-2 (strain SD95-21) are 129 KDa, 110 KDa, and 92 KDa, respectively (Fig. 1). However, in sodium do-decyl sulfate-polyacrylamide gel electrophoresis (SDS-PAGE), we ob-served that the apparent sizes of nsp2-related proteins were sub-stantially larger than the predicted molecular weights (Fang et al., 2012; Li et al., 2018). We therefore investigated whether post-transla-tional modifications, in particular phosphorylation, affect the mobilities of nsp2-related proteins in SDS-PAGE. Nsp2-related proteins were im-munoprecipitated (IP) from PRRSV-1 SD01-08-infected cells using a monoclonal antibody (mAb) that recognizes the N-terminal PLP2 do-main region, which is common to all three proteins (Fang et al., 2012;
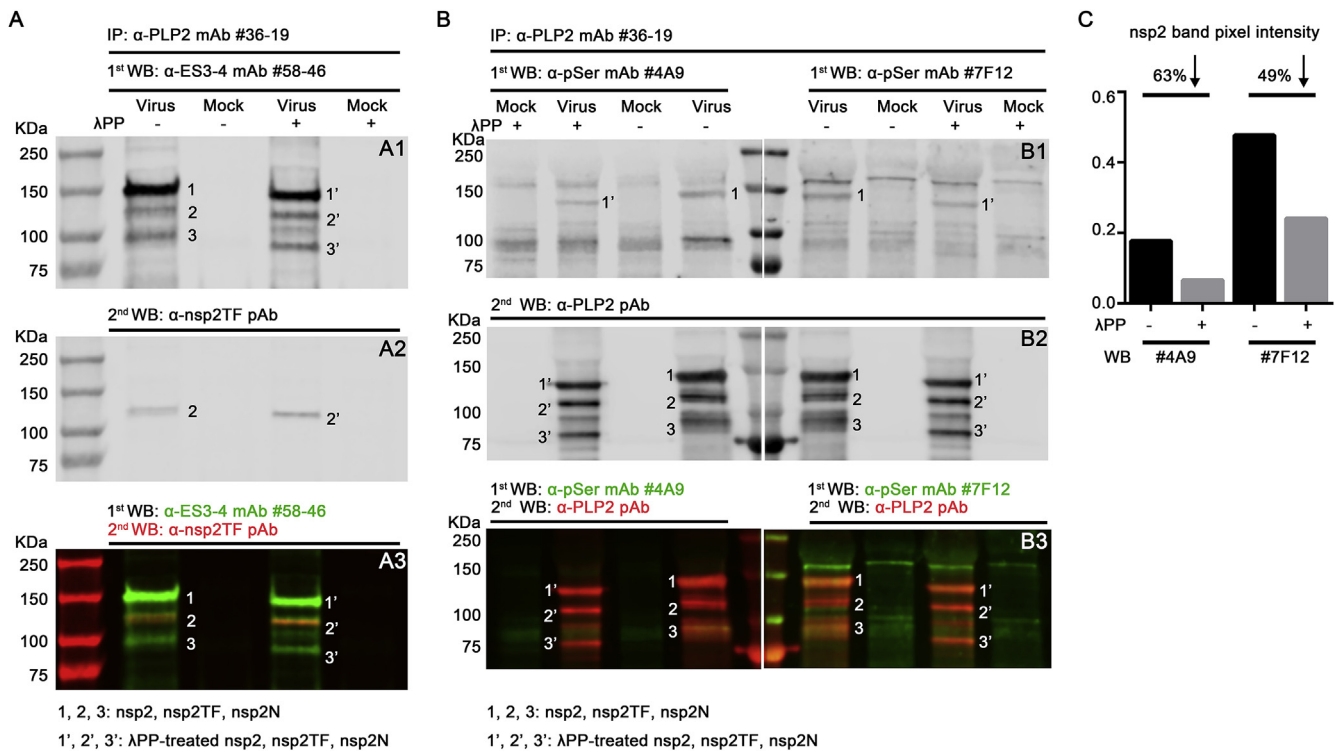
Fig. 2. Detection of phosphorylation on nsp2-related proteins of PRRSV-1. (**A**) Mobilities of phosphatase-treated proteins in SDS-polyacrylamide gel. Nsp2-related proteins bound on Sepharose beads were treated with λPP and separated by SDS-PAGE. Anti-PLP2 mAb #36–19 was used for immunoprecipitation (IP). Anti-ES3-4 mAb #58–46 and anti-nsp2TF pAb were used in Western blots to visualize apparent size changes with and without λPP treatment. (**B**) Western blot (WB) detection of phosphorylation status of nsp2-related proteins with λPP treatment. Anti-pSer mAbs-#4A9 and #7F12 were used to detect the phosphorylation status of the protein (shown as green fluorescent signal in panel B3). To confirm the specificities of pSer mAbs, a pAb recognizing nsp2-related proteins was also used in WB analysis (shown as red fluorescent signal panel B3). Each panel shows a WB membrane from the transfer of an SDS-PAGE gel. Following the transfer, the membrane was cut and probed with different antibodies. (**C**) Pixel intensities of nsp2 bands were calculated using Image Studio 5.2 (Li-Cor Biosciences).

Li et al., 2014). Immunoprecipitated proteins were treated with λ phosphatase (λPP) and compared to their untreated counterparts by SDS-PAGE and western blotting analysis. Dephosphorylation by λPP increased the apparent mobilities of all three nsp2-related proteins relative to the untreated samples (Fig. 2A), suggesting that the nsp2-related proteins are phosphorylated. Subsequently, we used a panel of anti-phosphoserine monoclonal antibodies (mAbs) to confirm the phosphorylation states of nsp2-related proteins. Anti-pSer mAbs #4A9 and #7F12 specifically recognized nsp2 protein, indicating that serine residues within nsp2 were phosphorylated. After λPP treatment, nsp2 bands with increased mobility were still recognized by mAbs #4A9 and #7F12 (Fig. 2B); however, the corresponding protein band intensities of the higher-mobility species of nsp2 were reduced by ~63% and ~49%, respectively (Fig. 2C), indicating that the complement of phosphorylated serine/threonine residues of nsp2 were partially dephosphorylated after λPP treatment, yielding hypo-phosphorylated nsp2-related proteins. It is noted that a new protein band appeared between nsp2TF and nsp2N after λPP treatment, but this band was not present before phosphatase treatment. We suspect that this may be another nsp2-derived variant with original size close to that of nsp2TF; after λPP treatment, this variant migrated differently than nsp2TF due to a different phosphorylation status.

To identify specific phosphorylation sites, we carried out mass spectrometric analysis of immunoprecipitated nsp2 and nsp2TF proteins. Since the N-terminal 714 amino acids are identical between nsp2 and Nsp2N (Fig. 1), we did not subject the latter to mass analysis. Mass spectrometric data showed that PRRSV nsp2 and nsp2TF are hyperphosphorylated at more than eighteen sites, including ambiguous sites (Table 1). Nsp2 contains eleven phosphorylation sites, while twelve sites in nsp2TF were identified. Mass spectrometric peptide analysis did not allow us to unambiguously distinguish between threonine^{896} and

serine^{897} in nsp2, or between serine^{1027} and threonine^{1029} in nsp2TF. Among the identified sites, up to fifteen phosphorylated residues are located between the PLP2 domain and the −2/−1 programmed frameshifting site. This region is present in all three nsp2-related proteins. Residues serine^{687}, serine^{838}, serine^{859}, serine^{863}, serine^{902} and serine^{1010} are unambiguously phosphorylated in both nsp2 and nsp2TF. Tyrosine^{1253}, threonine^{1373} and serine^{1440} are located in regions found only in nsp2, which include the predicted transmembrane (TM) domain and C-terminal domain. We assessed the conservation of these phosphorylation sites by quantifying their percentage of change in the genomes of other PRRSV isolates deposited in Genbank (Table 1). Serine^{579}, serine^{827}, serine^{838}, serine^{859}, serine^{863}, serine^{897}, serine^{918}, tyrosine^{1253} and serine^{1440} showed high conservation with less than 10% of changes (Table 1).

2.2. Mapping phosphorylation sites to functional domains of nsp2-related proteins

To obtain insights into potential consequences and effects of nsp2-related protein phosphorylation on viral replication, we closely analyzed the sequences of nsp2-related proteins. We focused in particular on identifying predicted functional and structural features of regions that contain key phosphorylated sites. The nsp2, nsp2TF and nsp2N proteins contain a relatively conserved PLP2 domain, a small hypervariable region (HVR-1) N-terminal to the PLP2 domain, and two large hypervariable regions (HVR-2 and HVR-3) between the PLP2 domain and the −2/-1 PRF site. The HVRs, by definition, diverge widely between species (Fang and Snijder, 2010; Snijder et al., 2013), but can be defined as distinct domains because they are separated by a more conserved domain. Sequence analysis and structural modeling of HVR-2 and HVR-3 showed that these regions have low sequence

Table 1
PRRSV-1 nsp2 and nsp2TF phosphorylation sites identification by mass spectrometry.

Nsp2 residues (position in pp1a/nsp2)	Mass spec identified peptide	Nsp2TF residue (position in pp1a/nsp2TF)	Mass spec identified peptide	Percentage of conservation	Localization in B-cell epitopes[&]
		S579/S194	TLDKMLT**S**PSPERSGF	3.4%	
		S667/S282	**S**PGAAVALCSPDAK	37.4%	
		T685/T300	SPDAKGFEG**T**ASEEAQESGHKA	77.5%	
S687/S302	GFEGTA**S**EEAQESGHK	S687/S302	GFEGTA**S**EEAQESGHK	84.7%	
		S827/S442	LDL**S**LAAW	1.7%	ES5
S838/S453	TA**S**DPGWVRG	S838/S453	AAWPVKATA**S**DPGW	0%	
	KATA**S**DPGWVRG		ATA**S**DPGWVR		
	TA**S**DPGWVR		KATA**S**DPGWVRG		
S859/S474	F**S**DGDSA	S859/S474	F**S**DGDSALQ	0%	
	F**S**DGDSALQFGEL		F**S**DGDSALQFGEL		
S863/S478	FSDGD**S**ALQFGELSES	S863/S478	FLKPRKAFSDGD**S**A	0%	
T896*/T511*	DAPVDLT**T**SNEALSA			23.1%	ES6
S897*/S512*	DAPVDLTT**S**NEALSAVDPS	S897/S512	DAPVDLTT**S**NEALSAVDPS	6.0%	ES6
	DAPVDLTT**S**NEALS		DAPVDLTT**S**NEALS		
	DAPVDLTT**S**NEAL				
S902/S517	DAPVDLTTSNEAL**S**AVDPS	S902/S517	DAPVDLTTSNEAL**S**AVDPS	10.3%	ES6
		S918/S533	H**S**AQALIDR	0%	ES6
S1010/S625	RA**S**DSAGLKQLVA	S1010/S625	RA**S**DSAGLKQLVA	25.6%	
	RA**S**DSAGLKQLV		RA**S**DSAGLKQL		
		S1027*/S642*	DKKL**S**VTPPPKSAGL	12%	ES7
			KL**S**VTPPPK		
T1029/T644	RWDKKLSV**T**PPPKSA	T1029*/T644*	RWDKKLSV**T**PPPKSAGL	27.4%	ES7
	DKKLSV**T**PPPKSAGL		DKKLSV**T**PPPKSAGL		
	SV**T**PPPKSAGL		SV**T**PPPKSAGL		
	SV**T**PPPKSA		KKLSV**T**PPPK		
	KLSV**T**PPPK		KLSV**T**PPPK		
	LSV**T**PPPK		SV**T**PPPKSA		
Y1253[#]/Y868[#]	ALSLV**Y**VVSQGR			0%	
T1373[#]/T988[#]	VLQAGGAIVDQP**T**PEVVR			14.4%	
S1440[#]/S1055[#]	NQTPLRDSA**S**TKTTGG			8.2%	
	LNQTPLRDSA**S**TKTTGGTK				

Amino acids with bold font: identified phosphorylation sites in peptide analysis; *: ambiguously identified phosphorylation sites; #: phosphorylation sites that only exist in ORF1a reading frame; & Epitope sites were identified from previous study (de Lima et al., 2006). Percentage of conservation is generated by comparing all the available PRRSV-1 sequences in GenBank as of November 26, 2019.

Table 2
Comparative analysis on intrinsically disordered regions between PLP2 and -2/-1 PRF

	HVR approximate positions (positions in pp1a)	Positions of putative IDRs between PLP2 and TM1 (positions in pp1a)				
		Pondr-FIT	Pondr VL-XT	DISOPRED3	MobiDB 3.0	metaPrDOS
PRRSV-1 nsp2 (SD01-08 strain)	HVR-2: 665aa-825aa	657aa-819aa	661aa-781aa	680aa-913aa	728aa-758aa	655aa-710aa
						727aa-780aa
						799aa-814aa
						863aa-900aa
	HVR-3: 1010aa-1085aa	998aa-1077aa	998aa-1075aa	1005aa-1079aa	1031aa-1064aa	1003aa-1066aa
PRRSV-2 nsp2 (VR-2332 strain)	HVR-2: 843aa-993aa	752aa-1014aa	628aa-661aa	683aa-739aa	809aa-856aa	751aa-770aa
			732aa-782aa	815aa-1017aa	899aa-936aa	813aa-1013aa
			807aa-852aa		948aa-979aa	
			865aa-1014aa			
	HVR-3: 1143aa-1213aa	1185aa-1222aa	1108aa-1227aa	1115aa-1205aa	1156aa-1221aa	1149aa-1213aa

complexity and a low probability to form stable secondary structures. Furthermore, HVR-2 and HVR-3 were consistently predicted to be intrinsically disordered by the disorder prediction algorithms Pondr-FIT, Pondr VL-XT (Bomma et al., 2012), DISOPRED3 (Jones and Cozzetto, 2014), MobiDB 3.0 (Piovesan et al., 2017) and metaPrDOS (Ishida and Kinoshita, 2008) (Table 2; Fig. 3). In contrast, a conserved region between HVR-2 and HVR-3 exhibits several consistent structural features (Fig. 3). Based on structure prediction and sequence variation analysis, we define this region as an independent structured domain, termed the inter-HVR-conserved domain (IHCD). The N-terminal portion of the IHCD is predicted to primarily adopt random coil conformations, with relatively little predicted secondary structure (Fig. 4A). The C-terminal portion of the IHCD is predicted to contain a structured fold putatively consisting of 4 or 5 helices (α1-α4 or α4'). Moreover, three short

peptides with uncharacteristically high inter-species conservation are present within the structured core (Fig. 4A; highlighted in grey color). Homology-based and *ab initio* structural modeling of the C-terminal portion of the IHCD using I-TASSER and Quark (Xu and Zhang, 2012; Yang et al., 2015), yields a number of helical bundle models with distinct topologies (Fig. 4B). A lack of proteins/domains of known structure and with high sequence similarity to the IHCD prevents us from evaluating the relative accuracy of these models. However, these models predict that extensive helix-helix interactions form a hydrophobic core and a stable, well-defined domain fold for the C-terminal portion of the IHCD. Of the phosphorylated residues described above, serine[667], threonine[685], and serine[687] are located within HVR-2, while serine[1010], serine[1027], and threonine[1029] are located within HVR-3. The N-terminal portion of the IHCD contains the phosphorylation sites
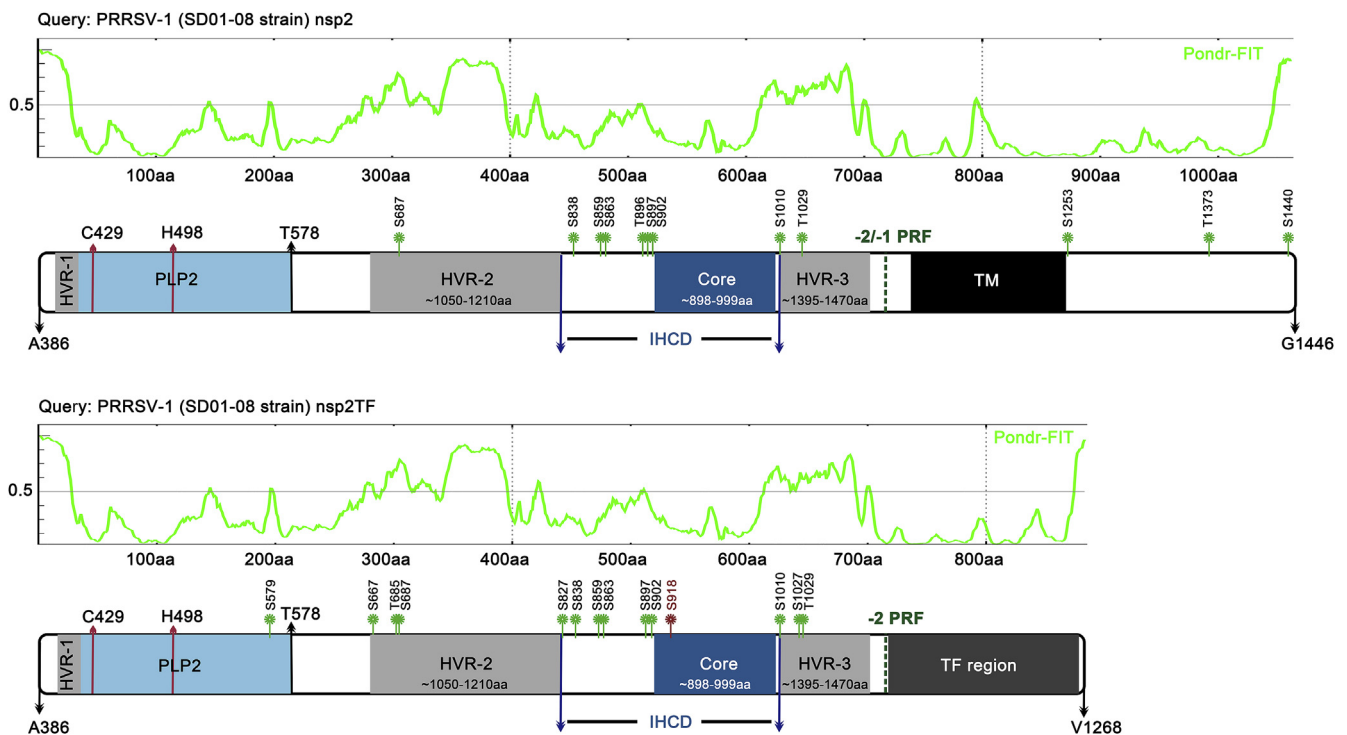
Fig. 3. Mapping phosphorylation sites to domains of nsp2-related proteins from PRRSV-1. Phosphorylation sites mapped to domains of nsp2 and nsp2TF are indicated by green or red markers. The red marker indicates the critical phosphorylation site-serine[918]. Light blue, grey, dark blue, and black shaded boxes indicate the PLP2, HVRs, IHCD structure core, and TM domains, respectively. The predicted sequence ranges for each domain are shown with numbering corresponding to ORF1a of PRRSV-1 SD 01–08. Green dashed vertical lines indicate -2/-1 PRF sites. Potential structural features and intrinsic disorder of nsp2 and nsp2TF were analyzed by using the Pondr-FIT program.

serine[827], serine[838], serine[859], serine[863], serine[897], and serine[902], while serine[918] is located in the C-terminal structured core of the IHCD (Fig. 3). Further in-depth sequence analysis showed that Serine[918] is located within the first inter-species short conserved motif (Fig. 4A).

2.3. Serine[918]-phosphorylation regulates viral infectious particle production and accumulation of subgenomic RNAs

To determine whether nsp2-related protein phosphorylation is involved in critical viral functions, we introduced phospho-ablatant mutations into a full-length cDNA infectious clone of PRRSV-1 SD01-08 (Li et al., 2013). We mutated the relevant serines or threonines to alanines and replaced tyrosines with phenylalanines. Each residue was changed individually, while adjacent mutations were also combined (Fig. 5). The phosphorylation site Tyr[1253] is located in a sequence that overlaps with the −2 ORF, although it is located within the nsp2-coding region. To avoid non-target mutation in the corresponding amino acid of nsp2TF, we introduced the Y1253F mutation into a previously constructed mutant (KO2), in which the expression of ns2TF and nsp2N was knocked out, but the nsp2 sequence was not affected (Fang et al., 2012). Using this panel of mutants, we first determined the impact of nsp2-related protein phosphorylation on viral production. The full-length cDNA infectious clone of each mutant was transfected into BHK-21 cells and cell culture supernatant was harvested at 48 h post transfection, followed by measurement of viral titer. Compared to the wild type virus, the mutant S918A showed the lowest viral yield, with the titer decreased by one log (Fig. 5).

We confirmed this result by determining the impact of serine[918] mutation on accumulation of viral genomic RNA (gRNA) and subgenomic RNA (sgRNA). Initially, viral RNA was transcribed from the T7 promoter-driven cDNA infectious clone of the S918A mutant and transfected into BHK-21 cells. The expression levels of both plus (+) and minus (−) strand gRNA and sgRNA were measured by qRT-PCR at

18 hpt. In comparison to the WT virus, the S918A mutant showed lower levels of (+) and (−) gRNA, with (+) and (−) mutant gRNA/WT gRNA ratios of 69.5% and 58.6%, respectively (Fig. 6A and B). The relative accumulations of three representative sgRNAs, sgRNA 2, 6 and 7, were significantly reduced in S918A transfected cells. The ratio of (+) sgRNA2/6/7 to (+) gRNA was reduced by 62.3%, 57.3%, and 47.6%, respectively (Fig. 6A). Similarly, the relative ratios of (−) sgRNA2/6/7 were reduced by 78.4%, 51.2%, and 60.1%, respectively (Fig. 6B). To further confirm the importance of S918 phosphorylation on viral RNA expression, a phospho-mimetic substitution S918E was included in this assay. As shown in Fig. 6, the S918E mutation showed higher levels of viral gRNA and sgRNA expression compared to that of S918A mutant. We obtained a similar result from virus-infected MARC-145 cells, in which S918A mutant showed large reduction in viral RNA expression compared to that of WT virus, while S918E mutant showed much less decrease in the level of viral RNA expression compared to the WT virus (Fig. S1). Reduced levels of viral RNAs should result in decreased expression of viral proteins. As expected, the expression levels of nonstructural protein (nsp1β) and structural protein (N protein) were decreased by about 52% and 64% in S918A mutant RNA transfected cells compared to those in WT virus (Fig. 7). In contrast, the accumulated levels of nsp1β and N protein were slightly decreased by the S918E mutation, with about 32% and 16% in S918E mutant infected cells compared to those in WT virus (Fig. 7).

Next, we compared the in vitro growth kinetics of S918 mutants to that of WT virus. PRRSV-permissive MARC-145 cells were infected with WT virus or a S918 mutant (passage 0). Cell cultural supernatants were harvested at selected time points post-infection and virus titers were determined. Compared to WT virus, S918A mutant showed significantly attenuated replication ability in MARC-145 cells (Fig. 8A). At 60 hpi, WT virus reached peak viral titer of 5.83 $\log_{10}$ FFU/ml, while S918A mutant reached a viral titer of 4.47 $\log_{10}$ FFU/ml. Consistent with the result of viral RNA expression levels, the S918E mutant showed viral
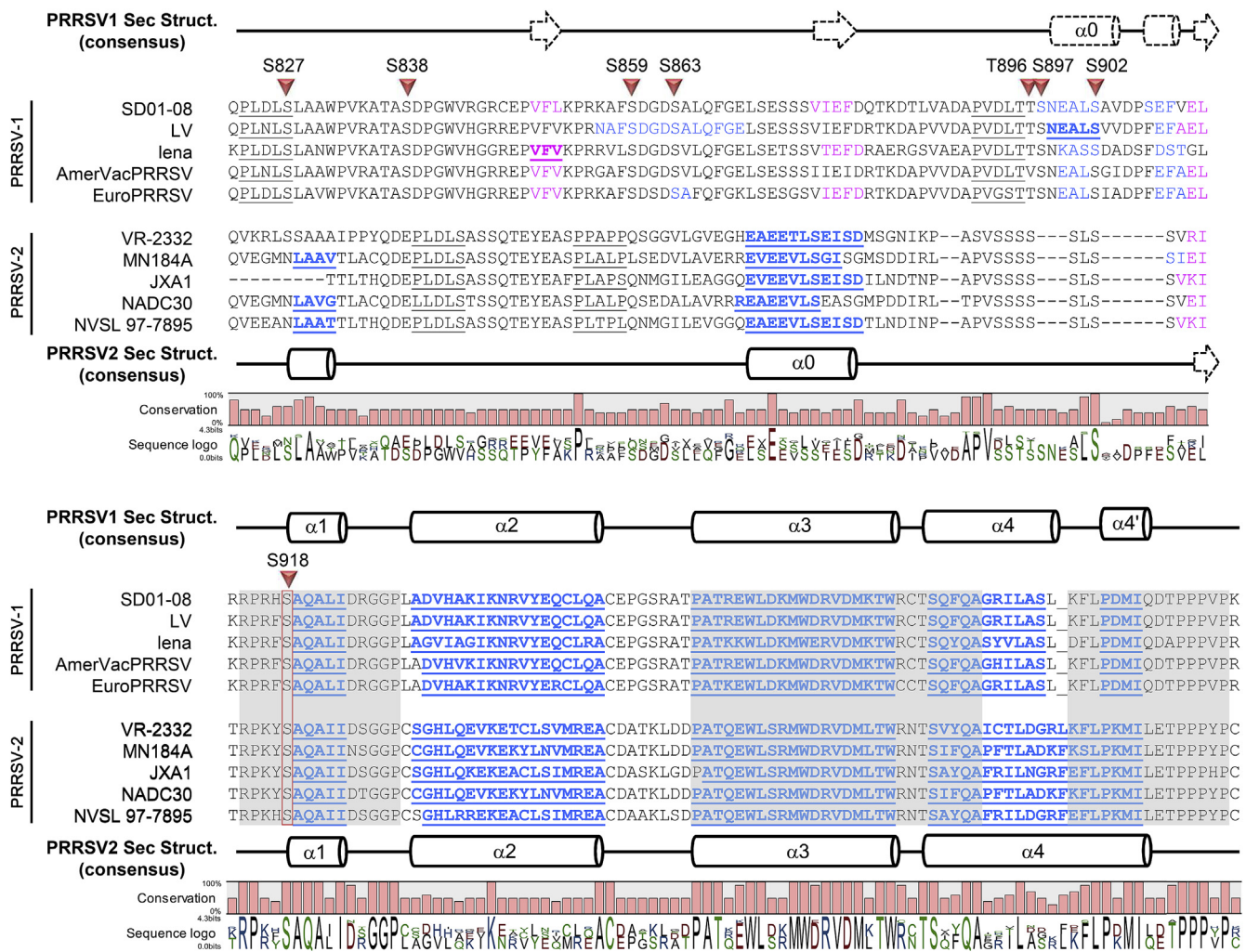
Fig. 4. Sequence analysis of inter-HVR conserved domain (IHCD) in PRRSV nsp2-related proteins. (**A**) IHCD regions from representative PRRSV strains were aligned in CLC Main Workbench 8.1 (CLC bio). Highly conserved sequences are highlighted by grey shading. Secondary structures predicted by I-TASSER modeling of PRRSV-1 and PRRSV-2 IHCD sequences are shown above or beneath corresponding amino acids (cylinders indicate α helices; arrows indicate β sheets). Sequences putatively corresponding to α-helix and β-sheet structures are shown in blue and magenta. Predicted structures with high confidence are highlighted in underlined bold font. Sequence conservation measure and logo obtained using CLC Main Workbench 8.1 (CLC bio) are shown underneath. Phosphorylation sites are labeled with red triangles. The critical phosphorylation site serine[918] is indicated by a red frame. Sequences of representative PRRSV strains were obtained from Genbank, including SD01-08 (Genbank DQ489311.1), Lelystad virus (LV) (Genbank M96262.2), lena (Genbank JF802085.1), Amervac PRRS (Genbank GU067771.1), EuroPRRSV (Genbank AY366525.1) and PRRSV-2 strains-VR-2332 (Genbank AY150564.1), MN184A (Genbank DQ176019.1), JXA1 (Genbank EF112445.1), NADC30 (Genbank JN654459.1), and NVSL 97–7895 (Genbank AY545985.1). (**B**) Representative structural predictions of the C-terminal structured region of the IHCD. B1 and B2 show homology models of PRRSV-1/2 sequences. Similar I-TASSER homology modeling predictions from multiple PRRSV-1 and/or PRRSV-2 family members are shown superimposed and colored in a blue-to-red spectrum (N-terminus to C-terminus of modeled sequence). B3 and B4 are *ab initio* predicted models including helical bundles and super-helical (helix-of-helices) arrangement for of PRRSV-1/2 sequences.
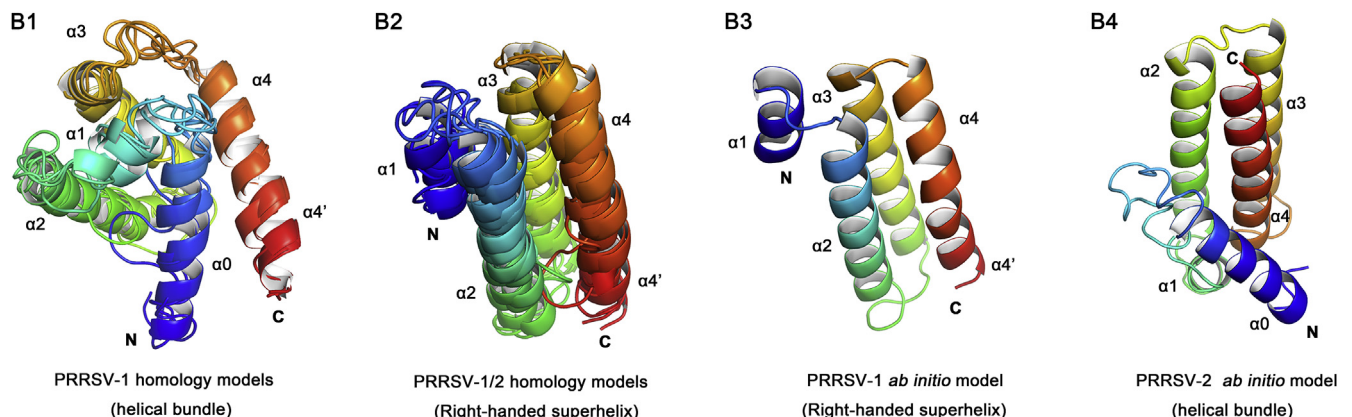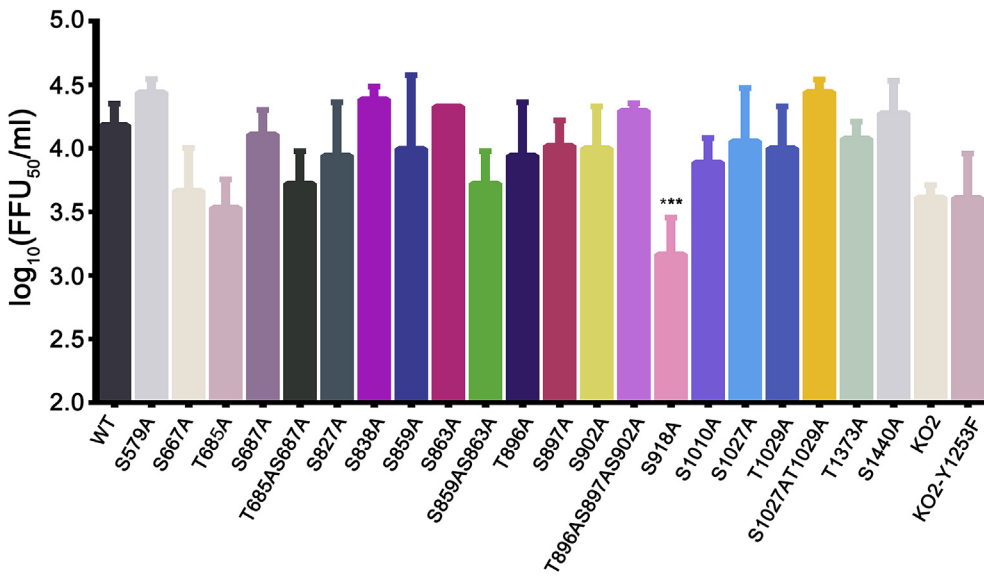
B1 PRRSV-1 homology models (helical bundle)

B2 PRRSV-1/2 homology models (Right-handed superhelix)

B3 PRRSV-1 *ab initio* model (Right-handed superhelix)

B4 PRRSV-2 *ab initio* model (helical bundle)

Fig. 4. (*continued*)

Fig. 5. Rescue efficiencies of phospho-ablatant mutants. Individual PRRSV cDNA infectious clones of phospho-ablatant mutation were individually transfected into BHK-21 cells. Cell culture supernatants were harvested 48 h post transfection and virus titers were determined. Each data point represents the mean value of triplicates.
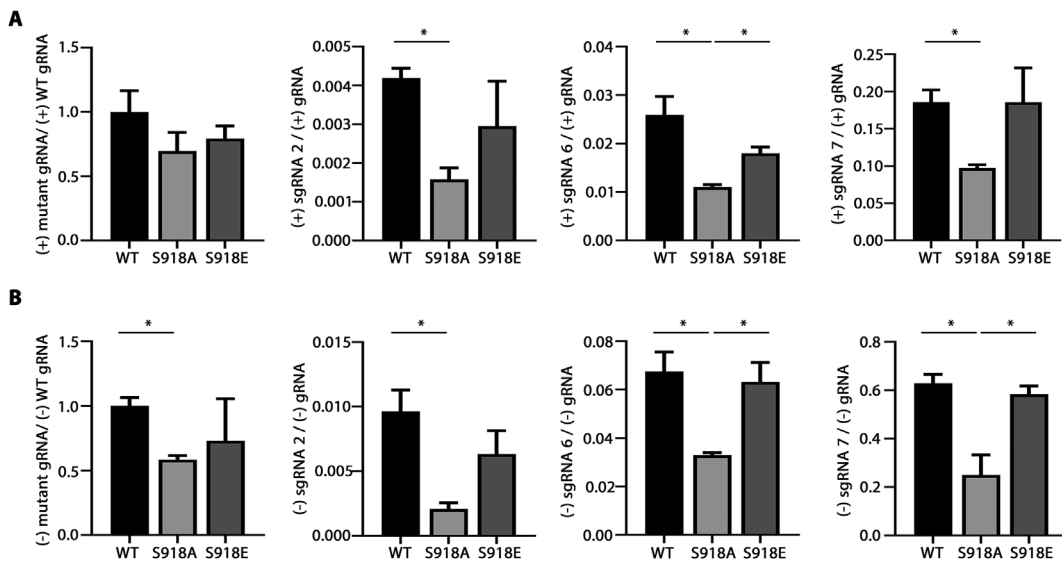
Fig. 6. Phosphorylation at serine^{918} influences relative accumulation of viral RNAs. *In vitro* transcribed genomic RNA of WT virus and mutants S918A and S918E were transfected into BHK-21 cells. At 18 h post transfection, BHK-21 cells were lysed and qRT-PCR was performed using the specific primers and probes (Table S1, Fig. S3) to quantify the plus and minus genomic RNA and subgenomic RNA. Ratios of plus-strand (A) and minus-strand (B) RNA were calculated by ΔΔCt method (Pfaffl, 2007; Rao et al., 2013). Each data point represents the mean value of triplicates. *: $p < 0.05$.

growth ability greater than that of the S918A mutant, with higher peak viral titer (5.01 log$_{10}$ FFU/ml) at 60 hpi. The cytolytic ability of mutant S918A was severely attenuated with no visible plaque detected in MARC-145 cells at 4 days post infection (Fig. 8B). IFA results confirmed

that the S918A mutant infected the cells; however, this mutant resulted in smaller viral clusters than the WT virus. In contrast, S918E mutant exhibited higher growth ability with visible plaques and larger viral clusters than that observed for S918A mutant (Fig. 8B and C).
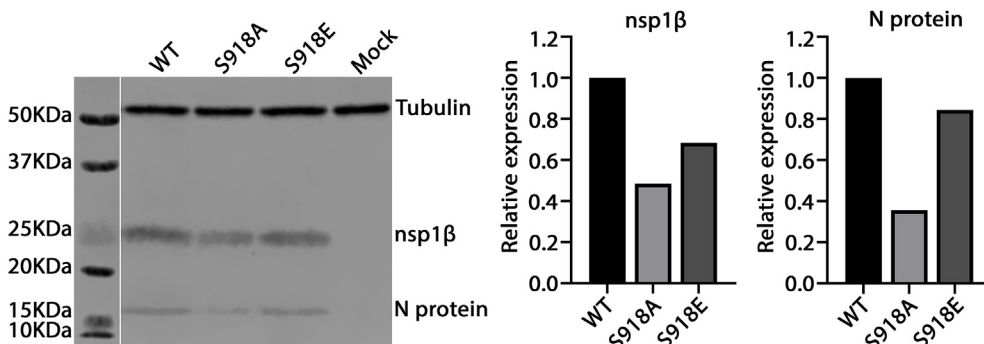
Fig. 7. Effect of serine^{918} phosphorylation on viral nonstructural and structural protein expression. *In vitro* transcribed genomic RNA of WT virus and mutants S918A and S918E were transfected into BHK-21 cells. Expression of viral nsp1β and N protein in BHK-21 cells at 18 h post transfection was detected by western blotting using α-nsp1β mAb #22–28 and α-N mAb #14–126. Pixel intensity was quantified using Image Studio 5.2 (Li-Cor Biosciences). Normalization was performed using a monoclonal antibody specific for the host cell housekeeping protein Tubulin.
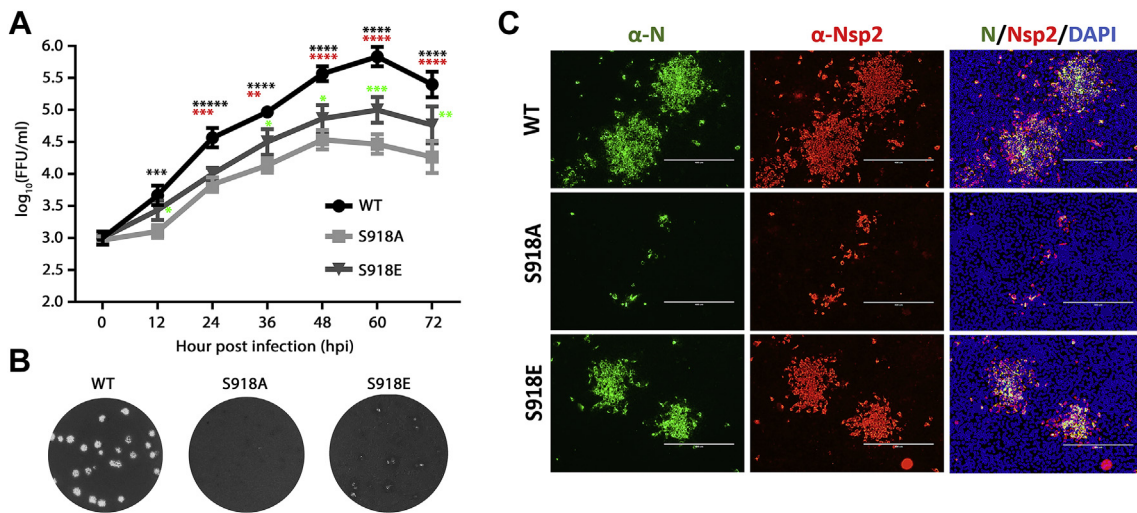
Fig. 8. Growth characterization of S918 mutants in MARC-145 cells. (**A**) Growth kinetics of WT virus, and S918A and S918E mutants in MARC-145 cells. Cells were infected by each virus (passage 0) at 0.01 moi, and cell culture supernatants were harvested and titrated every 12 h post infection. Black *: WT vs S918A; Green *: S918E vs S918A; Red *: WT vs S918E; *: $p < 0.05$; **: $p < 0.01$; ***: $p < 0.001$; ****: $p < 0.0001$. (**B**) Plaque morphology of WT and S918 mutants in MARC-145 cells. Confluent cell monolayers were infected with a 10-fold serially diluted WT or mutant virus. At 2 hpi, medium was removed, and a low-melting agar was overlaid on the top of the cells. Cells were incubated at 37°C for 4 days and then stained by 0.1% crystal violet to visualize the plaque formation. (**C**) Immunofluorescent assay to detect viral infection in MARC-145 cells. Cells were infected by each virus (passage 0) at 0.01 moi and fixed at 48 hpi. Infected cells were immunostained for PRRSV nsp2 or N protein. The nsp2 was labeled with red fluorescence, and N was labeled with green fluorescence, while DAPI (purple) was used to stain the cell nucleus. Pictures were taken by a confocal microscope (Nikon A1R; Nikon). Scale bars, 400 μm.
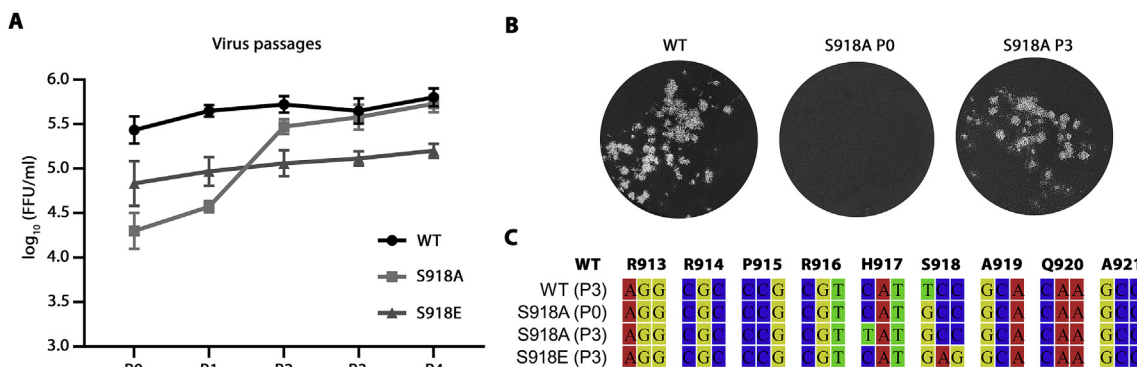
Fig. 9. Comparison of virus titers in different passages of WT virus and S918 mutants. At each passage, MARC-145 cells were infected by the WT or mutant virus at 0.01 moi, and cell cultural supernatant was harvested at 48 hpi. Virus titer was determined by counting the virus foci under the fluorescence microscope, and the result was interpreted as the number of fluorescent focus units per mL (FFU/mL).

Stabilities of these mutants were further studied by serially passaging the viruses in cell culture. At passage 2, we observed a significant increase of viral titer for the S918A mutant (4.57 $\log_{10}$ FFU/ml at P1 versus 5.47 $\log_{10}$ FFU/ml at P2), which reached levels similar to those of WT virus at P3 and P4 (Fig. 9A). At P3, the S918A mutant showed similar plaque size as that of the WT virus in infected cells (Fig. 9B), apparently recovering from its initially impaired growth ability caused by mutating the S918 phosphorylation site. Sequencing analysis of the nsp2 region showed that the S918A mutation is stable through different passages. However, we detected a second site mutation at amino acid 917 of nsp2 (H917Y, next to S918A), starting from passage 2 (Fig. 9C). The sequence RRPRYAAQA generated from the second site mutation is a predicted phosphorylation site of Tyrosine kinase, suggesting that the H917Y mutation may provide an alternative, functionally redundant phosphorylation site to the site eliminated by S918A mutation. These results further confirm the important role of S918 phosphorylation in the viral replication.

3. Discussion

As the most ubiquitous form of post-translational modification, protein phosphorylation modulates essentially all fundamental biological activities in a cell (Humphrey et al., 2015; Hunter, 1995; Johnson, 2009; Tarrant and Cole, 2009; Ubersax and Ferrell, 2007). Viruses exploit host phosphorylation mechanisms to carry out critical viral functions and processes, including survival and replication (Keating and Striker, 2012; Keck et al., 2015). The effects of phosphorylation of viral proteins on viral replication are broadly reported and have been characterized in both RNA and DNA viruses (Keating and Striker, 2012; Keck et al., 2015). Previous characterization of protein phosphorylation in nidoviruses, including murine hepatitis virus (MHV), infectious bronchitis virus (IBV), transmissible gastroenteritis coronavirus (TGEV), severe acute respiratory syndrome coronavirus (SARS-CoV), equine arteritis virus (EAV), and PRRSV focused exclusively on the N proteins of these viruses (McBride et al., 2014; Wu et al., 2009; White et al., 2007; Surjit et al., 2005; Stohlman and Lai, 1979; Spencer et al., 2008; Peng et al., 2008; Mohandas and Dales, 1991; Chen et al., 2005; Chang et al., 2009; Calvo et al., 2005; Zeegers et al., 1976). The

biological consequences of such phosphorylation events on viral replication were extensively investigated in coronaviruses (McBride et al., 2014). For example, the phosphorylation state of the IBV N protein regulates its affinity for the viral leader sequence, suggesting that phosphorylation regulates RNA transcription in IBV (Spencer et al., 2008; Chen et al., 2005). Phosphorylation by the host GSK3 kinase affects conformational transitions of the MHV N protein and regulates its interaction with the DDX1 helicase to fine-tune the discontinuous transcription of sgRNAs (Wu et al., 2014). Phosphorylation of the N protein of PRRSV has also been reported (Wootton et al., 2002; Yoo et al., 2003; Chen et al., 2018, 2019). Phospho-ablatant mutations on two PRRSV N protein phosphorylation sites attenuated viral replication capability both *in vitro* and *in vivo* (Chen et al., 2018, 2019). However, specific biological roles of PRRSV N protein phosphorylation remain largely unclear.

In our study, we demonstrate for the first time the importance of phosphorylation of PRRSV proteins other than N protein in viral replication. We determined that PRRSV nsp2-related protein phosphorylation critically modulates viral RNA expression, especially expression levels of sgRNAs. Previous studies demonstrated that nsp2 plays a primary role in viral replication by proteolytically processing replicase polyproteins through its PLP2 domain (Wassenaar et al., 1997). Arterivirus nsp2 was also reported to play an important role in the formation of double membrane vesicles (DMVs) that anchor the replication transcription complex (Snijder et al., 2001, 2013; Posthuma et al., 2008). The identification of two additional frameshifting products, nsp2TF and nsp2N, increases the functional versatility and also the complexity of potential roles played by nsp2 (Snijder et al., 2013; Fang et al., 2012; Li et al., 2014, 2018). We observed that all three nsp2-related proteins (nsp2, nsp2TF and nsp2N) are phosphorylated. Mutations introduced into the phosphorylation site serine^{918} (S918A) attenuated viral replication *in vitro*. In particular, disrupting the phosphorylation status of serine^{918} significantly downregulates steady-state levels of viral sgRNAs accumulation. Whether nsp2-related proteins, working as trans-acting factor(s), directly regulate arterivirus discontinuous transcription warrants further investigation. In PRRSV-infected cells, nsp2TF exhibits a different subcellular localization pattern than that of nsp2 (Fang et al., 2012). This suggests that the phosphorylation state of these proteins may regulate viral replication in different contexts, by different mechanisms, or that not all of the nsp2-related proteins are involved in sgRNA synthesis.

Compared with other conserved domains in nsp2-related proteins, the region between the PLP2 domain and −2/−1 PRF site is poorly defined in terms of structure and function. Based on sequence and structural prediction analysis, we subdivided this large region into two HVRs separated by a relatively conserved inter-HVR region that contains a highly conserved domain (IHCD) in both PRRSV-1 and PRRSV-2. Previous studies examined the consequences of deletions introduced into segments that overlap with the HVRs and the IHCD. In PRRSV-1 (strain SD01-08), HVR-2 contains two known immuno-dominant epitopes, ES3 (residues 691–722 of pp1a) and ES4 (residues 736–790 of pp1a). HVR-3 contains the epitope ES7 (residues 1015–1040 of pp1a), while another epitope, ES5 (residues 822–832 of pp1a) is located within the N-terminal portion of the IHCD. In addition, the epitope ES6 (residues 895–923 of pp1a) is located at the junction of two portions of the IHCD (Oleksiewicz et al., 2001; Chen et al., 2010) (Fig. 4). Our previous studies demonstrated that deletion of the ES3 epitope caused enhanced cytolysis and more vigorous *in vitro* growth kinetics, while ES4 and ES7 deletion mutants exhibited attenuated *in vitro* growth properties. In contrast, deletion of epitopes ES5 and ES6, located within the IHCD, was lethal and no viable virus was rescued. *In vivo* characterization of ES3, ES4, and ES7 deletion mutants in infected pigs showed levels of viremia consistent with the *in vitro* effects of epitope deletion. In addition, mRNA and protein expression levels of IL-1β and TNF-α were downregulated in ES3 deletion mutant-infected macrophages (Chen et al., 2010). Another study identified specific regions of

nsp2 that are dispensable for replication of PRRSV-2 (strain VR-2332) (Han et al., 2007). Deletion of residues 707–906 in pp1a (residues 324–523 in nsp2) and 926–1015 in pp1a (residues 543–632 in nsp2), which overlap with HVR-2, resulted in viable recombinant viruses, but incurred severe fitness loss. Similarly, deletion of 1016–1109 in pp1a (residues 633–726 in nsp2), and 1110–1196 in pp1a (residues 727–813 in nsp2), which respectively overlap with the IHCD and partially overlap with HVR-3, also had severe effects on viral fitness (Han et al., 2007). Furthermore, a deletion in the IHCD C-terminal portion (residues 1011–1130 of pp1a) that occurred naturally during an *in vitro* passage attenuated a highly pathogenic PRRSV-2 strain to an avirulent vaccine strain-TJM (F92) (Leng et al., 2012). These results indicate that HVR-2/HVR-3 and IHCD potentially interact with the host immune system and that these regions are associated with viral fitness and replication ability.

In the current study, mass-spectrometric analysis of PRRSV-1 identified that most of the phosphorylation sites are located in the HVRs and inter-HVR regions, in which nsp2 contains 6 phosphorylated sites and nsp2TF contains 7 sites. As described above, PRRSV nsp2-related proteins are enriched with immune-dominant B-cell epitopes, as well as predicted T-cell epitopes (Snijder et al., 2013; Oleksiewicz et al., 2001; Chen et al., 2010; de Lima et al., 2006; Fang et al., 2004). Interestingly, serine^{827} is located in epitope ES5; threonine^{896} (or serine^{897}), serine^{902} and serine^{918} are located in epitope ES6, and serine^{1027} and threonine^{1029} are located within epitope ES7 (Table 1). We previously demonstrated that the epitopes ES5, ES6, and ES7 in IHCD must be fully intact for the viability or fitness of the virus (Chen et al., 2010). The functional importance of nsp2 phosphorylation sites other than serine^{918} needs to be further elucidated.

Our sequence analysis showed that the region between the PLP2 domain and PRF site contains intrinsic disordered regions (IDRs), which have only low levels of sequence similarity to any other known proteins or protein domains. To investigate whether the hypervariable and potentially disordered nature of these regions in PRRSV apply to other arteriviruses, we used Pondr VL-XT software (Bomma et al., 2012) to analyze the sequences of representative species of five genera in the family *Arteriviridae* (Gulyaeva et al., 2017). In all of these species, regions between the PLP2 and the putative transmembrane region TM1 are predicted to contain IDRs of variable length (Fig. S2). Structural flexibility in the segments between PLP2 and TM1 seems to represent a general property of the nsp2-related proteins of the arterivirus family. In general, IDRs and IDPs (intrinsic disordered proteins) lack hydrophobic residues to support formation of well-defined and folded hydrophobic cores and do not adopt stable tertiary structures in the absence of binding partners (Wright and Dyson, 2015; Van Der Lee et al., 2014; Oldfield and Dunker, 2014; Uversky, 2013; Dyson and Wright, 2005). Conformations of IDPs/IDRs are more typically represented as dynamic ensembles. Such disordered regions can present highly diversified binding sites for other macromolecular partners. As intracellular parasites, the life cycle of viruses depends critically upon interactions between viral proteins and host components. The absence of strong structural constraints correlates with less restriction on sequence selection and higher tolerance to sequence substitution, promoting sequence variability (Van Der Lee et al., 2014; Oldfield and Dunker, 2014; Uversky, 2013; Xue et al., 2014; Gitlin et al., 2014). Furthermore, looser constraints on conformation permit dynamic display of post-translational modification sites, including phosphorylation sites, to facilitate transient interactions with modifying enzymes. Similarly, structural flexibility allows for ready access and recognition of modified sites for downstream interactions (Van Der Lee et al., 2014; Oldfield and Dunker, 2014; Uversky, 2013).

The functional consequences of structural disorder are commonly found in the proteomes of viruses, especially for RNA viruses (Wright and Dyson, 2015; Van Der Lee et al., 2014; Oldfield and Dunker, 2014; Uversky, 2013; Dyson and Wright, 2005; Xue et al., 2014). Structural flexibility can endow viral proteins from compact RNA genome with the

ability to carry out multiple functions in viral life cycles, and is compatible with the low-fidelity transcription typically mediated by viral RNA polymerases (Van Der Lee et al., 2014; Xue et al., 2014). For example, the Hepatitis C virus nonstructural protein NS5A contains two disordered domains (D2 and D3), which are believed to serve as protein-protein interaction (PPI) hubs (Shanmugam et al., 2018; Badillo et al., 2017; Sólyom et al., 2015). The D2 domain interacts with the RNA-dependent RNA polymerase NS5B and the host innate immune receptor Protein Kinase R (Shanmugam et al., 2018; Badillo et al., 2017; Sólyom et al., 2015). Both D2 and D3 domains mediate the interaction between NS5A and the critical host factor cyclophilin A (CypA), facilitating the formation of an NS5A-NS5B transcription and replication complex. The disordered D2 domain tolerates large deletions without obvious fitness loss. In alphaviruses, the c-terminal region of nsP3 proteins contain a large hypervariable domain, which is also mostly disordered and hyper-phosphorylated (Götte et al., 2018; Frolov et al., 2017; Rupp et al., 2015). The nsP3 plays critical roles in the formation of viral replication complexes (vRCs) and also regulates RNA transcription. The HVD of nsP3 is enriched with functional PPI motifs, including a Src homology 2 (SH2) domain-binding YXXM motif that interacts with the PI3K-Akt-mTOR pathway and an SH3 domain-binding PXPXPR motif that interacts with host proteins of the amphiphysin family (Götte et al., 2018; Rupp et al., 2015). Importantly, repetitive motifs in the nsP3 HVD mediate critical binding to host stress granule (SG) proteins including G3BP1/2 and/or FXR family proteins (Götte et al., 2018; Frolov et al., 2017; Rupp et al., 2015). A growing number of studies show that disordered HVDs serve as PPI hubs, contributing to viral adaptation to the host environment, viral fitness and pathogenicity (Götte et al., 2018; Frolov et al., 2017; Chetan et al., 2018). In the case of PRRSV nsp2-related proteins, the two large putative IDRs associated with the HVRs and hyper-phosphorylation sites support the notion of a functional connection between sequence variability and mechanistic roles. Given that nsp2-related proteins contain the most apparent disordered regions in the viral proteome, the hyper-phosphorylated IDRs in nsp2-related proteins may function as evolutionary "hot-spots" for rapid adaptation to changing host environments, including immunological and physiological conditions, and to the very diverse range of host genetic backgrounds.

The disordered HVRs are separated by a conserved sequence region that we termed the inter-HVR conserved domain (IHCD). Unlike the HVRs, the C-terminal portion of the IHCD is likely to have a stable tertiary structure. Both homology modeling and *ab initio* structural predictions suggest that the C-terminal ~100 residues of this region are primarily alpha-helical and that the helices pack as a bundle. The topology of the overall fold cannot be unambiguously predicted as multiple topologies allow for plausible helix packing and a buried hydrophobic core. However, all the prediction software generated similar results for the PRRSV-1 and PRRSV-2 sequences, suggesting that this region likely adopts a common domain fold in both species. In contrast to the C-terminal structured domain, the N-terminal ~70–80 residues of the IHCD are predicted to contain little canonical secondary structure and may be conformationally dynamic or may adopt atypical tertiary structures. These sequences are relatively conserved within the PRRSV-1 and PRRSV-2 species. The conserved disorder and paucity of canonical secondary structure may be required for accessibility of the sequences to specific trans-acting factors and binding partners, including specific kinases that target the high density of phosphorylation sites in this region. It is noteworthy that the N-terminal portions of the IHCDs of PRRSV-1 and -2 sequences contain several instances of so-called PXDLS motifs. These linear motifs serve as binding sites for C-terminal binding proteins (CtBPs) (Chinnadurai, 2007), which may potentially link nsp2-related proteins to CtBP-associated host chromatin regulators or transcription factors. The interaction of nsp2 proteins with CtBP was previously reported in two interactome studies on highly pathogenic Chinese PRRSV-2 strains (Wang et al., 2014; Xiao et al., 2016). To obtain further insight into the functional and mechanistic properties of

the IDRs in HVR-2 and HVR-3, and the N-terminal portion of the IHCD, additional work will be needed to identify potential host interacting partners for these regions. Moreover, it will be important to characterize how phosphorylation near or within these segments modulates dynamic ensemble properties and protein-protein interactions of the HVRs and IHCD, and to correlate these to their effects on viral properties. The structured portion of the IHCD will need to be similarly investigated for several potential roles, including scaffolding or protein-protein interactions with other nsp2 domains, with other PRRSV gene products and with host protein factors.

4. Materials and methods

Cells, viruses: BHK-21 cells and MARC-145 cells were cultured in minimum essential medium (MEM) (Gibco, Carlsbad, CA) supplemented with 10% fetal bovine serum (FBS) (Sigma-Aldrich, St. Louis, MO) at 37˚C with 5% CO2. For the maintenance of infected MARC-145 cells, 10% FBS was replaced by 2% horse serum (HyClone, Logan, UT). The PRRSV-1 strain (SD01-08) was used in the following experiments. SD01-08 was isolated in 2001 in the US and subsequently used to construct full-length cDNA infectious clones (Fang et al., 2006; Li et al., 2013).

Antibodies: All PRRSV-1 specific antibodies used in this study were targeted to the strain SD01-08. Monoclonal antibodies (α-nsp2 mAbs #36–19 and #58–46, α-N mAb #14–126, and α-nsp1β mAb #22–28) and polyclonal antibody (pAb) against the PLP2 domain were generated as described in our previous studies (Fang et al., 2012; Li et al., 2012; Guo et al., 2016). The pAb specifically recognizes the TF peptide of nsp2TF was generated by GenScript Biotech Corporation (Piscataway, NJ) as we described previously (Fang et al., 2012). A panel of six specific anti-phosphorylated serine (pSer) mAbs was from a phosphoserine detection kit (Enzo Life Sciences, Ann Arbor, MI). The secondary antibodies, IRDye 800CW-conjugated goat anti-mouse IgG (H + L) and IRDye 680RD-conjugated goat anti-rabbit IgG (H + L), were purchased from Li-Cor Biosciences (Lincoln, NE), while Alexa-488 conjugated goat anti-mouse IgG and Alexa-594 conjugated goat anti-rabbit IgG were purchased from Jackson Immunoresearch (West Grove, PA). The anti-tubulin mAb (B-7) was obtained from Santa Cruz Biotechnology (Dallas, TX).

Mass spectrometric analysis: PRRSV nsp2-related proteins were pulled down from PRRSV-infected MARC-145 cells by immunoprecipitation (IP) as described previously (Fang et al., 2012). Virus-infected or mock-infected cells were harvested in lysis buffer (150 mM NaCl, 10 mM Tris-HCl, 1 mM EDTA, 1% NP-40, 0.5% sodium deoxycholate, 0.1% SDS) supplemented with Halt™ Protease and Phosphatase Inhibitor Cocktail (Thermo Fisher Scientific, Carlsbad, CA). To remove non-specifically bound proteins, cell lysates were pre-cleared with protein A Sepharose CL-4B beads (GE Healthcare Bio-Sciences, Pittsburgh, PA) and a non-specific mouse mAb at room temperature (RT) for 1 h. After brief centrifugation, cleared supernatant was transferred to a fresh tube containing mAb #36–19 and fresh Sepharose CL-4B beads. The mAb-protein complex was incubated with constant rotation at 4˚C overnight. The sepharose beads were washed six times with wash buffer (150 mM NaCl, 10 mM Tris-HCl, 1 mM EDTA, 1% NP-40, 0.5% sodium deoxycholate), followed by six washes with MiliQ water. Bound proteins were eluted and denatured in 2x Laemmli sample buffer (Bio-Rad, Hercules, CA) at 95˚C for 10 min. PRRSV nsp2-related proteins were separated and analyzed by SDS-PAGE gel, fixed, and stained with Coomassie brilliant blue G-250 (Bio-Rad Laboratories, Hercules, CA). Bands corresponding to PRRSV nsp2 and nsp2TF were excised from the gel and subjected to mass spectrometric analysis. Phosphorylation analysis was performed at the Harvard Microchemistry and Proteomics Analysis Facility by microcapillary reverse-phase HPLC nano-electrospray tandem mass spectrometry (µLC/MS/MS) on a Thermo LTQ-Orbitrap mass spectrometer.

Immuno-detection of phosphorylated nsp2-related proteins

and assessment of protein mobility in SDS-PAGE: Immunoprecipitated proteins were separated by SDS-PAGE and transferred onto nitrocellulose (NC) membranes (GE Healthcare Bio-Sciences, Pittsburgh, PA). A manufacturer recommended protocol was applied for phosphorylation immuno-detection using specific anti-pSer mAbs. Phosphate-buffered saline (PBS) with 1% BSA (MP Biochemical, Solon, OH), 1% PVP-10 (polyvinyl-pyrrolidone) (Sigma-Aldrich, St. Louis, MO), 1% PEG 3500 (Sigma-Aldrich, St. Louis, MO), and 0.2% Tween 20 (Sigma-Aldrich, St. Louis, MO) was used as blocking buffer and antibody diluent. NC membranes were blocked for 2 h at RT and incubated with diluted primary antibody for 1 h at RT. After three washes with 1x PBST (0.05% Tween-20), membranes were incubated with secondary antibodies for 45 min at RT. Following three washes with 1x PBST (0.05% Tween-20), protein bands were visualized using an Odyssey Fc imaging system (Li-Cor Biosciences, Lincoln, NE). Equivalent incubation and wash procedures were applied to membranes after a second incubation with antibodies against nsp2-related proteins. To assess differential mobilities of phosphatase-treated proteins in SDS-polyacrylamide gels, proteins bound to Sepharose beads in the IP process were dephosphorylated using Lambda Protein Phosphatase (λPP) (New England BioLabs, Ipswich, MA) at 30˚C for 2 h. In control samples, λPP was replaced by an equal volume of water. Migration of nsp2-related proteins after treatment was evaluated by SDS-PAGE and Western blot using the methods described previously (Li et al., 2014; Shang et al., 2017).

PRRSV reverse genetics for generating recombinant viruses: Site-directed mutations were introduced into the coding region of nsp2-related proteins of a PRRSV SD01–08 full-length cDNA infectious clone, pCMV-SD01-08, as described previously (Li et al., 2013). To recover the cloned virus, BHK-21 cells were transfected with the cDNA infectious clone of the wild type (WT) virus or its mutant. Transfection was conducted using Lipofectamine 3000 (Invitrogen, Carlsbad, CA) following the manufacturer's instructions. At 48 h post transfection, cell culture supernatant was harvested and designated as passage 0 (P0) of the virus.

***In vitro* growth characterization of recombinant viruses:** Each recombinant virus was serially passaged on MARC-145 cells 4 times. At each passage, cells were infected by each virus at multiplicity of infection (moi) of 0.01. Virus titers were measured by fluorescent-focus assay on MARC-145 cells and calculated as fluorescent focus units per mL (FFU/mL) using the method described previously (Sun et al., 2012). The specific mutation was confirmed by Sanger sequencing of the entire nsp2 region. *In vitro* growth kinetics of WT and mutant viruses (P0) were determined by infecting MARC-145 cells at 0.01 moi. Supernatants of infected cells were collected at 0, 12, 24, 36, 48, 60, and 72 h post-infection (hpi) and virus titers were measured by fluorescent-focus assay as described previously (Sun et al., 2012). Plaque morphologies of the WT and mutant viruses were compared by a plaque assay as described previously (Fang et al., 2012). Fluorescent images were taken under a confocal microscope (Nikon A1R HD25, Nikon).

***In vitro* transcription**: The plasmid DNA of full-length cDNA infectious clone pSD01-08 (Fang et al., 2006) was linearized by *Xba*I, and the digested DNA was extracted using phenol extraction and ethanol precipitation method. Linearized DNA (2 µg) was used as template for *in vitro* RNA transcription. *In vitro* transcription was performed in 50 µl reaction condition at 37 ˚C for 2 h: 5 µl RNAPol Reaction Buffer (New England BioLabs, Ipswich, MA), 5 µl ATP (10 mM), 5 µl UTP (10 mM), 5 µl CTP (10 mM), 2.5 µl GTP (10 mM) (New England BioLabs, Ipswich, MA), 7.5 µl m7G(5′)ppp(5′)G RNA Cap Structure Analog (10 mM) (New England BioLabs, Ipswich, MA), 2 µl T7 RNA Polymerase (New England BioLabs, Ipswich, MA), 2 µg linearized infectious clone plasmid, 2 µl RNaseOUT™ RNase inhibitor (Invitrogen, Carlsbad, CA). Then, 2 µl TURBO™ DNase (Invitrogen, Carlsbad, CA) was added into the reaction system to digest DNA templates for 30 min at 37 ˚C. Newly transcribed RNAs were purified by NucAway™ Spin Columns (Invitrogen, Carlsbad, CA) according to manufacturer's instruction. Subsequently, *in vitro*

transcribed RNAs (1.5 µg) were transfected into BHK-21 cells using Lipofectamine™ MessengerMAX™ Transfection Reagent (Thermo Fisher Scientific) with a 1:4 ratio of genomic RNA to MessengerMAX. Cell lysate and supernatant were collected at 18 post transfection (hpt).

Genomic and subgenomic viral RNA quantification: For RNA quantification, cellular total RNAs were extracted using the SV Total RNA Isolation kit (Promega, Madison, WI). Equal amounts (1.5 µg) of total RNAs were reverse transcribed using the Maxima H Minus Reverse Transcriptase (Thermo Fisher Scientific). Plus-strand genomic RNA, plus-strand subgenomic RNA, and minus-strand genomic/subgenomic RNA were reverse transcribed in three different reactions using three different primers (Table S1, Fig. S3). Real-time PCR was performed in 20 µl reactions containing 10 µl TaqMan™ Fast Advanced Master Mix (Applied Biosystems, Carlsbad, CA), 0.25 µl forward primer (40 µM), 0.25 µl reverse primer (40 µM), 0.4 µl Taqman probe (10 µM), 2 µl cDNA, 7.1 µl H_2O. Primer/probe sets were synthesized by Biosearch Technologies (Petaluma, CA). PCR reactions were performed on a CFX96 Touch™ Real-Time PCR Detection System (Bio-Rad, Hercules, CA). The PCR protocol was selected based on TaqMan™ Fast Advanced Master Mix user's instructions: 50 ˚C UNG incubation for 2 min, 95 ˚C polymerase activation for 2 min, followed by 40 cycles of denaturation cycles at 95 ˚C for 3 s and annealing/extention at 60 ˚C for 30 s. The relative accumulation ratio of RNAs was quantified by the threshold cycle ($_{\Delta\Delta}$CT) method (Pfaffl, 2007; Rao et al., 2013). To precisely quantify RNA accumulation and to rule out possible background interference from initial transfected RNA, we constructed a replication-defective mutant, in which the nucleotide sequence from 495 nt to 515 nt was replaced with 7 consecutive stop codons to terminate translation of nonstructural polyproteins. The (+) gRNA detected from BHK-21 cells transfected with the defective mutant (+) gRNA was designated as background. For (+) gRNA quantification, the background signal derived from transfection was first subtracted.

Sequence analysis and protein structure prediction: Multiple sequence alignments were performed using the built-in ClustalW program of CLC Main Workbench 8.1 (CLC bio, Aarhus, Denmark). Intrinsic disorder prediction was conducted using multiple online programs including Pondr-FIT (Xue et al., 2010), Pondr VL-XT (Bomma et al., 2012), DISOPRED3 (Jones and Cozzetto, 2014), MobiDB 3.0 (Piovesan et al., 2017), and metaPrDOS (Ishida and Kinoshita, 2008). Protein secondary structure profiles and tertiary structure predictions were generated by homology modeling using I-TASSER (Yang et al., 2015). For homology modeling, no template models were provided as input. Each PRRSV-1 and PRRSV-2 species member sequence was modeled independently, and a consensus secondary structure profile was generated based on these predictions. Models with C-scores better than −3.0 were assessed further and grouped by overall structural similarity. *Ab initio* models for each sequence were also generated using Quark (Xu and Zhang, 2012). Predictions were assessed according to I-Tasser/Quark scoring (1–10 scale), with individual residue scores of 4–5 designated as "low-confidence" and 6–10 as "high-confidence". Predicted structural models of similar topology and overall structure were evaluated, aligned and figures were generated using open-source PyMol 1.7 (The PyMol Molecular Graphics System, Version 1.7 Schrödinger, LLC).

Statistical significance analysis: All data in current study were shown as mean values with standard deviations. Each data represents three replicates. Statistical significance was evaluated by one-way analysis of variance (ANOVA) followed by Tukey's post hoc test using GraphPad Prism 6 (GraphPad, La Jolla, CA). P-values were indicated by asterisks in figures. *: $P < 0.05$, **:$P < 0.01$, ***:$P < 0.001$, ****: $P < 0.0001$, *****: $P < 0.00001$.

CRediT authorship contribution statement

Pengcheng Shang: Conceptualization, Methodology, Formal analysis, Writing - original draft. **Fangfeng Yuan:** Methodology, Formal

analysis. **Saurav Misra:** Formal analysis, Writing - review & editing. **Yanhua Li:** Methodology, Formal analysis. **Ying Fang:** Conceptualization, Funding acquisition, Supervision, Writing - review & editing.

Declaration of competing interest

The authors declare that they have no known competing financial interests or personal relationships that could have appeared to influence the work reported in this paper.

Acknowledgement

Appendix A. Supplementary data

Supplementary data to this article can be found online at https://doi.org/10.1016/j.virol.2020.01.018.

References

Badillo, A., Receveur-Brechot, Vr, Sp, Sarrazin, Cantrelle, Fo-X, Fdr, Delolme, Fogeron, M.-L., Molle, J., Montserret, R., Bockmann, A., Bartenschlager, R., 2017. Overall structural model of NS5A protein from Hepatitis C Virus and modulation by mutations confering resistance of virus replication to cyclosporin A. Biochemistry 56, 3029–3048.

Bomma, R., Venkatesh, P., Dlvnsssr, A., Babu, A., Rao, S., 2012. PONDR (predicators of natural disorder regions). Int. J. Comput. Technol. Electron. Eng. IJCTEE 2, 1–10.

Calvo, E., Escors, D., Lopez, J., Gonzalez, J., Alvarez, A., Arza, E., Enjuanes, L., 2005. Phosphorylation and subcellular localization of transmissible gastroenteritis virus nucleocapsid protein in infected cells. J. Gen. Virol. 86, 2255–2267.

Chang, C.-K., Hsu, Y.-L., Chang, Y.-H., Chao, F.-A., Wu, M.-C., Huang, Y.-S., Hu, C.-K., Huang, T.-H., 2009. Multiple nucleic acid binding sites and intrinsic disorder of severe acute respiratory syndrome coronavirus nucleocapsid protein: implications for ribonucleocapsid protein packaging. J. Virol. 83, 2255–2264.

Chen, H., Gill, A., Dove, B.K., Emmett, S.R., Kemp, C.F., Ritchie, M.A., Dee, M., Hiscox, J.A., 2005. Mass spectroscopic characterization of the coronavirus infectious bronchitis virus nucleoprotein and elucidation of the role of phosphorylation in RNA binding by using surface plasmon resonance. J. Virol. 79, 1164–1179.

Chen, Z., Zhou, X., Lunney, J.K., Lawson, S., Sun, Z., Brown, E., Christopher-Hennings, J., Knudsen, D., Nelson, E., Fang, Y., 2010. Immunodominant epitopes in nsp2 of porcine reproductive and respiratory syndrome virus are dispensable for replication, but play an important role in modulation of the host immune response. J. Gen. Virol. 91, 1047–1057.

Chen, Y., Xing, X., Li, Q., Feng, S., Han, X., He, S., Zhang, G., 2018. Serine 105 and 120 are important phosphorylation sites for porcine reproductive and respiratory syndrome virus N protein function. Vet. Microbiol. 219, 128–135.

Chen, Y., Yu, Z., Yi, H., Wei, Y., Han, X., Li, Q., Ji, C., Huang, J., Deng, Q., Liu, Y., 2019. The phosphorylation of the N protein could affect PRRSV virulence in vivo. Vet. Microbiol.

Chetan, D., Meshram, P.A., Shiliaev, Nikita, Urakova, Nadya, Mobley, James A., Agback, Tatiana, Frolova, Elena I., Frolov, Ilya, 2018. Multiple host factors interact with hypervariable domain of chikungunya virus nsP3 and determine viral replication in cell-specific mode. J. Virol. 92.

Chinnadurai, G., 2007. Transcriptional regulation by C-terminal binding proteins. Int. J. Biochem. Cell Biol. 39, 1593–1607.

de Lima, M., Pattnaik, A., Flores, E., Osorio, F., 2006. Mapping of B-cell linear epitopes on Nsp2 and structural proteins of a North American strain of porcine reproductive and respiratory syndrome virus. Virology 353, 410–421.

Dyson, H.J., Wright, P.E., 2005. Intrinsically unstructured proteins and their functions. Nat. Rev. Mol. Cell Biol. 6, 197.

Fang, Y., Snijder, E.J., 2010. The PRRSV replicase: exploring the multifunctionality of an intriguing set of nonstructural proteins. Virus Res. 154, 61–76.

Fang, Y., Kim, D.-Y., Ropp, S., Steen, P., Christopher-Hennings, J., Nelson, E.A., Rowland, R.R., 2004. Heterogeneity in Nsp2 of European-like porcine reproductive and respiratory syndrome viruses isolated in the United States. Virus Res. 100, 229–235.

Fang, Y., Rowland, R.R., Roof, M., Lunney, J.K., Christopher-Hennings, J., Nelson, E.A., 2006. A full-length cDNA infectious clone of North American type 1 porcine reproductive and respiratory syndrome virus: expression of green fluorescent protein in the Nsp2 region. J. Virol. 80, 11447–11455.

Fang, Y., Treffers, E.E., Li, Y., Tas, A., Sun, Z., Van Der Meer, Y., De Ru, A.H., Van Veelen, P.A., Atkins, J.F., Snijder, E.J., 2012. Efficient − 2 frameshifting by mammalian ribosomes to synthesize an additional arterivirus protein. Proc. Natl. Acad. Sci. Unit.

States Am. 109, E2920–E2928.

Frias-Staheli, N., Giannakopoulos, N.V., Kikkert, M., Taylor, S.L., Bridgen, A., Paragas, J., Richt, J.A., Rowland, R.R., Schmaljohn, C.S., Lenschow, D.J., 2007. Ovarian tumor domain-containing viral proteases evade ubiquitin-and ISG15-dependent innate immune responses. Cell Host Microbe 2, 404–416.

Frolov, I., Akhrymuk, M., Mobley, J.A., Frolova, E.I., 2017. Hypervariable domain of eastern equine encephalitis virus nsP3 redundantly utilizes multiple cellular proteins for replication complex assembly. J. Virol. 91 e00371-17.

Gitlin, L., Hagai, T., LaBarbera, A., Solovey, M., Andino, R., 2014. Rapid evolution of virus sequences in intrinsically disordered protein regions. PLoS Pathog. 10, e1004529.

Götte, B., Liu, L., McInerney, G.M., 2018. The enigmatic alphavirus non-structural protein 3 (nsP3) revealing its secrets at last. Viruses 10, 105.

Gulyaeva, A., Dunowska, M., Hoogendoorn, E., Giles, J., Samborskiy, D., Gorbalenya, A.E., 2017. Domain organization and evolution of the highly divergent 5′ coding region of genomes of arteriviruses, including the novel possum nidovirus. J. Virol. 91 e02096-16.

Guo, R., Katz, B.B., Tomich, J.M., Gallagher, T., Fang, Y., 2016. Porcine reproductive and respiratory syndrome virus utilizes nanotubes for intercellular spread. J. Virol. 90, 5163–5175.

Han, J., Liu, G., Wang, Y., Faaberg, K.S., 2007. Identification of nonessential regions of the nsp2 replicase protein of porcine reproductive and respiratory syndrome virus strain VR-2332 for replication in cell culture. J. Virol. 81, 9878–9890.

Han, J., Rutherford, M.S., Faaberg, K.S., 2010. Proteolytic products of the porcine reproductive and respiratory syndrome virus nsp2 replicase protein. J. Virol. 84, 10102–10112.

Humphrey, S.J., James, D.E., Mann, M., 2015. Protein phosphorylation: a major switch mechanism for metabolic regulation. Trends Endocrinol. Metabol. 26, 676–687.

Hunter, T., 1995. Protein kinases and phosphatases: the yin and yang of protein phosphorylation and signaling. Cell 80, 225–236.

Ishida, T., Kinoshita, K., 2008. Prediction of disordered regions in proteins based on the meta approach. Bioinformatics 24, 1344–1348.

Johnson, L.N., 2009. The regulation of protein phosphorylation. Biochem. Soc. Trans. 37, 627–641.

Jones, D.T., Cozzetto, D., 2014. DISOPRED3: precise disordered region predictions with annotated protein-binding activity. Bioinformatics 31, 857–863.

Keating, J.A., Striker, R., 2012. Phosphorylation events during viral infections provide potential therapeutic targets. Rev. Med. Virol. 22, 166–181.

Keck, F., Ateay, P., Amaya, M., Bailey, C., Narayanan, A., 2015. Phosphorylation of single stranded RNA virus proteins and potential for novel therapeutic strategies. Viruses 7, 5257–5273.

Kuhn, J.H., Lauck, M., Bailey, A.L., Shchetinin, A.M., Vishnevskaya, T.V., Bào, Y., Ng, T.F.F., LeBreton, M., Schneider, B.S., Gillis, A., 2016. Reorganization and expansion of the nidoviral family Arteriviridae. Arch. Virol. 161, 755–768.

Leng, X., Li, Z., Xia, M., He, Y., Wu, H., 2012. Evaluation of the efficacy of an attenuated live vaccine against highly pathogenic porcine reproductive and respiratory syndrome virus (HP-PRRSV) in young pigs. Clin. Vaccine Immunol.:CVI 05646-11.

Li, Y., Tas, A., Snijder, E.J., Fang, Y., 2012. Identification of porcine reproductive and respiratory syndrome virus ORF1a-encoded non-structural proteins in virus-infected cells. J. Gen. Virol. 93, 829–839.

Li, Y., Zhu, L., Lawson, S.R., Fang, Y., 2013. Targeted mutations in a highly conserved motif of the nsp1β protein impair the interferon antagonizing activity of porcine reproductive and respiratory syndrome virus. J. Gen. Virol. 94, 1972–1983.

Li, Y., Treffers, E.E., Napthine, S., Tas, A., Zhu, L., Sun, Z., Bell, S., Mark, B.L., van Veelen, P.A., van Hemert, M.J., 2014. Transactivation of programmed ribosomal frameshifting by a viral protein. Proc. Natl. Acad. Sci. Unit. States Am. 111, E2172–E2181.

Li, Y., Shang, P., Shyu, D., Carrillo, C., Naraghi-Arani, P., Jaing, C.J., Renukaradhya, G., Firth, A., Snijder, E., Fang, Y., 2018. Nonstructural proteins nsp2TF and nsp2N of porcine reproductive and respiratory syndrome virus (PRRSV) play important roles in suppressing host innate immune responses. Virology.

McBride, R., van Zyl, M., Fielding, B.C., 2014. The coronavirus nucleocapsid is a multifunctional protein. Viruses 6, 2991–3018.

Mohandas, D.V., Dales, S., 1991. Endosomal association of a protein phosphatase with high dephosphorylating activity against a coronavirus nucleocapsid protein. FEBS Lett. 282, 419–424.

Oldfield, C.J., Dunker, A.K., 2014. Intrinsically disordered proteins and intrinsically disordered protein regions. Annu. Rev. Biochem. 83, 553–584.

Oleksiewicz, M., Bøtner, A., Toft, P., Normann, P., Storgaard, T., 2001. Epitope mapping porcine reproductive and respiratory syndrome virus by phage display: the nsp2 fragment of the replicase polyprotein contains a cluster of B-cell epitopes. J. Virol. 75, 3277–3290.

Peng, T.Y., Lee, K.R., Tarn, W.Y., 2008. Phosphorylation of the arginine/serine dipeptide-rich motif of the severe acute respiratory syndrome coronavirus nucleocapsid protein modulates its multimerization, translation inhibitory activity and cellular localization. FEBS J. 275, 4152–4163.

Pfaffl, M.W., 2007. Relative quantification. In: Real-time PCR. Taylor & Francis, pp. 89–108.

Piovesan, D., Tabaro, F., Paladin, L., Necci, M., Mičetić, I., Camilloni, C., Davey, N., Dosztányi, Z., Mészáros, B., Monzon, A.M., 2017. MobiDB 3.0: more annotations for intrinsic disorder, conformational diversity and interactions in proteins. Nucleic Acids Res. 46, D471–D476.

Posthuma, C.C., Pedersen, K.W., Lu, Z., Joosten, R.G., Roos, N., Zevenhoven-Dobbe, J.C., Snijder, E.J., 2008. Formation of the arterivirus replication/transcription complex: a key role for nonstructural protein 3 in the remodeling of intracellular membranes. J. Virol. 82, 4480–4491.

Rao, X., Huang, X., Zhou, Z., Lin, X., 2013. An improvement of the 2ˆ (–delta delta CT)

method for quantitative real-time polymerase chain reaction data analysis. Biostat., Bioinf. Biomath. 3, 71.

Rupp, J.C., Sokoloski, K.J., Gebhart, N.N., Hardy, R.W., 2015. Alphavirus RNA synthesis and non-structural protein functions. J. Gen. Virol. 96, 2483–2500.

Shang, P., Misra, S., Hause, B., Fang, Y., 2017. A naturally occurring recombinant enterovirus expresses a torovirus deubiquitinase. J. Virol. 91 e00450-17.

Shanmugam, S., Nichols, A.K., Saravanabalaji, D., Welsch, C., Yi, M., 2018. HCV NS5A dimer interface residues regulate HCV replication by controlling its self-interaction, hyperphosphorylation, subcellular localization and interaction with cyclophilin A. PLoS Pathog. 14, e1007177.

Snijder, E.J., van Tol, H., Roos, N., Pedersen, K.W., 2001. Non-structural proteins 2 and 3 interact to modify host cell membranes during the formation of the arterivirus replication complex. J. Gen. Virol. 82, 985–994.

Snijder, E.J., Kikkert, M., Fang, Y., 2013. Arterivirus molecular biology and pathogenesis. J. Gen. Virol. 94, 2141–2163.

Sólyom, Z., Ma, P., Schwarten, M., Bosco, M., Polidori, A., Durand, G., Willbold, D., Brutscher, B., 2015. The disordered region of the HCV protein NS5A: conformational dynamics, SH3 binding, and phosphorylation. Biophys. J. 109, 1483–1496.

Spencer, K.-A., Dee, M., Britton, P., Hiscox, J.A., 2008. Role of phosphorylation clusters in the biology of the coronavirus infectious bronchitis virus nucleocapsid protein. Virology 370, 373–381.

Stohlman, S., Lai, M., 1979. Phosphoproteins of murine hepatitis viruses. J. Virol. 32, 672–675.

Sun, Z., Chen, Z., Lawson, S.R., Fang, Y., 2010. The cysteine protease domain of porcine reproductive and respiratory syndrome virus nonstructural protein 2 possesses deubiquitinating and interferon antagonism functions. J. Virol. 84, 7832–7846.

Sun, Z., Li, Y., Ransburgh, R., Snijder, E.J., Fang, Y., 2012. Nonstructural protein 2 of porcine reproductive and respiratory syndrome virus inhibits the antiviral function of interferon-stimulated gene 15. J. Virol. 86, 3839–3850.

Surjit, M., Kumar, R., Mishra, R.N., Reddy, M.K., Chow, V.T., Lal, S.K., 2005. The severe acute respiratory syndrome coronavirus nucleocapsid protein is phosphorylated and localizes in the cytoplasm by 14-3-3-mediated translocation. J. Virol. 79, 11476–11486.

Tarrant, M.K., Cole, P.A., 2009. The chemical biology of protein phosphorylation. Annu. Rev. Biochem. 78, 797–825.

Ubersax, J.A., Ferrell Jr., J.E., 2007. Mechanisms of specificity in protein phosphorylation. Nat. Rev. Mol. Cell Biol. 8, 530.

Uversky, V.N., 2013. A decade and a half of protein intrinsic disorder: biology still waits for physics. Protein Sci. 22, 693–724.

Van Der Lee, R., Buljan, M., Lang, B., Weatheritt, R.J., Daughdrill, G.W., Dunker, A.K., Fuxreiter, M., Gough, J., Gsponer, J., Jones, D.T., 2014. Classification of intrinsically disordered regions and proteins. Chem. Rev. 114, 6589–6631.

van Kasteren, P.B., Beugeling, C., Ninaber, D.K., Frias-Staheli, N., van Boheemen, S.,

García-Sastre, A., Snijder, E.J., Kikkert, M., 2012. Arterivirus and nairovirus ovarian tumor domain-containing deubiquitinases target activated RIG-I to control innate immune signaling. J. Virol. 86, 773–785.

Wang, L., Zhou, L., Zhang, H., Li, Y., Ge, X., Guo, X., Yu, K., Yang, H., 2014. Interactome profile of the host cellular proteins and the nonstructural protein 2 of porcine reproductive and respiratory syndrome virus. PloS One 9, e99176.

Wassenaar, A., Spaan, W., Gorbalenya, A.E., Snijder, E.J., 1997. Alternative proteolytic processing of the arterivirus replicase ORF1a polyprotein: evidence that NSP2 acts as a cofactor for the NSP4 serine protease. J. Virol. 71, 9313–9322.

White, T.C., Yi, Z., Hogue, B.G., 2007. Identification of mouse hepatitis coronavirus A59 nucleocapsid protein phosphorylation sites. Virus Res. 126, 139–148.

Wootton, S.K., Rowland, R.R., Yoo, D., 2002. Phosphorylation of the porcine reproductive and respiratory syndrome virus nucleocapsid protein. J. Virol. 76, 10569–10576.

Wright, P.E., Dyson, H.J., 2015. Intrinsically disordered proteins in cellular signalling and regulation. Nat. Rev. Mol. Cell Biol. 16, 18.

Wu, C.-H., Yeh, S.-H., Tsay, Y.-G., Shieh, Y.-H., Kao, C.-L., Chen, Y.-S., Wang, S.-H., Kuo, T.-J., Chen, D.-S., Chen, P.-J., 2009. Glycogen synthase kinase-3 regulates the phosphorylation of severe acute respiratory syndrome coronavirus nucleocapsid protein and viral replication. J. Biol. Chem. 284, 5229–5239.

Wu, C.-H., Chen, P.-J., Yeh, S.-H., 2014. Nucleocapsid phosphorylation and RNA helicase DDX1 recruitment enables coronavirus transition from discontinuous to continuous transcription. Cell Host Microbe 16, 462–472.

Xiao, Y., Wu, W., Gao, J., Smith, N., Burkard, C., Xia, D., Zhang, M., Wang, C., Archibald, A., Digard, P., 2016. Characterization of the interactome of the porcine reproductive and respiratory syndrome virus nonstructural protein 2 reveals the hyper variable region as a binding platform for association with 14–3–3 proteins. J. Proteome Res. 15, 1388–1401.

Xu, D., Zhang, Y., 2012. Ab initio protein structure assembly using continuous structure fragments and optimized knowledge-based force field. Proteins: Structure, Function, and Bioinformatics 80, 1715–1735.

Xue, B., Dunbrack, R.L., Williams, R.W., Dunker, A.K., Uversky, V.N., 2010. PONDR-FIT: a meta-predictor of intrinsically disordered amino acids. Biochim. Biophys. Acta Protein Proteonomics 1804, 996–1010.

Xue, B., Blocquel, D., Habchi, J., Uversky, A.V., Kurgan, L., Uversky, V.N., Longhi, S., 2014. Structural disorder in viral proteins. Chem. Rev. 114, 6880–6911.

Yang, J., Yan, R., Roy, A., Xu, D., Poisson, J., Zhang, Y., 2015. The I-TASSER Suite: protein structure and function prediction. Nat. Methods 12, 7.

Yoo, D., Wootton, S.K., Li, G., Song, C., Rowland, R.R., 2003. Colocalization and interaction of the porcine arterivirus nucleocapsid protein with the small nucleolar RNA-associated protein fibrillarin. J. Virol. 77, 12173–12183.

Zeegers, J., Van der Zeijst, B., Horzinek, M., 1976. The structural proteins of equine arteritis virus. Virology 73, 200–205.